Journal of Magnetic Resonance 193 (2008) 286–296

Contents lists available at ScienceDirect

Journal of Magnetic Resonance

journal homepage: www.elsevier.com/locate/jmr

Microstructural analysis of foam by use of NMR R_2 dispersion

S.H. Baete [a,b,*,1], Y. De Deene [a,b,1], B. Masschaele [c], W. De Neve [a]

[a] Department of Radiotherapy, Ghent University Hospital, De Pintelaan 185, 9000 Gent, Belgium
[b] MEDISIP-IBBT, Ghent University, De Pintelaan 185, 9000 Gent, Belgium
[c] Department of Subatomic and Radiation Physics, Ghent University, Proeftuinstraat 86, 9000 Gent, Belgium

ARTICLE INFO

Article history:
Received 4 April 2008
Revised 9 May 2008
Available online 20 May 2008

Keywords:
Quantitative magnetic resonance imaging
Microstructure
R_2-dispersion
Relaxometry
Foam
Random walk
Internal gradients
Surface relaxation

ABSTRACT

The spin–spin relaxation rate R_2 (=1/T_2) in hydrogel foams measured by use of a multiple spin echo sequence is found to be dependent on the echo time spacing. This property, referred to as R_2-dispersion, originates to a large extent from molecular self-diffusion of water within internal field gradients that result from magnetic susceptibility differences between the gel and air phase. Another contribution to the R_2 relaxation rate is surface relaxation. Numerical simulations are performed to investigate the relation between the foam microstructure (the mean air bubble radius and standard deviation of the air bubble radius) and foam composition properties (such as magnetic susceptibilities, diffusion coefficient and surface relaxivity) at one hand and the R_2-dispersion at the other hand. The simulated R_2-dispersions of gel foam are in agreement with the measured R_2-dispersions. By correlating the R_2-dispersion parameters and simulated microstructure properties a semi-empirical relationship is obtained that enables the mean air bubble size to be derived from measured R_2-dispersion curves. The R_2-derived mean air bubble size of a hydrogel foam is in agreement with the bubble size measured with X-ray micro-CT. This illustrates the feasibility of using ^{1}H R_2-dispersion measurements to determine the size of air bubbles in hydrogel foams and of alveoli in lung tissue.

1. Introduction

Quantitative MRI (qMRI) facilitates the follow-up and treatment of pathological tissue. Moreover, quantitative MRI can provide quantitative information about tissue microstructure. However, because of the interplay of different contrast parameters, the correlation between microstructure properties of human tissue and MR contrast parameters is not always straightforward. Numerical simulations and simple experimental model systems can help in getting an insight in these correlations. In this study, the correlation between the structural and composition-related properties of foam and the measured transverse relaxation rate R_2 is examined. This study can be regarded as a proof-of-principle of a non-invasive method for the determination of the size of alveoli in lungs by ^{1}H MRI.

In previous studies, the underlying lung geometry has been correlated with NMR proton spectra (e.g. [1]) and with the difference of a pair of signals recorded with a symmetric and an asymmetric spin echo sequence [2]. Both methods rely on the magnetic field inhomogeneities induced by susceptibility differences across the alveolar air–tissue interface. In this study, we use the combined effect of magnetic field inhomogeneities and surface relaxation on the measured spin–spin relaxation rate (R_2). The effect is illustrated in hydrogel foams. It is shown through X-ray micro-CT that these hydrogel foams mimic lung tissue very well. A hydrogel foam is a biphasic system consisting of air bubbles separated by thin films containing hydrogel and Plateau borders (triangular borders where three or more bubbles meet [3]).

From an NMR point-of-view, the hydrogel foam and lung tissue can be considered as a porous medium (Fig. 1a). The R_2 in the porous system is increased by the surface relaxation (R_{2S}) and by a term accounting for the molecular self-diffusion of the water molecules in the inhomogeneous internal field which is caused by differences in magnetic susceptibility (χ) between the gel phase and the gas phase (R_{2IG}, IG for internal gradients). Both relaxation terms can be used to determine characteristical dimensions of microstructure geometry [4–23].

A random walk simulation [6,24–28] is used to study the relation between the mean air bubble radii and the R_2-dispersion curve (R_2 as a function of echo time spacing ΔTE). The effect of other composition-related parameters such as magnetic susceptibility differences, water diffusion coefficient and surface relaxivity has also been investigated. The simulated R_2-dispersion curves are parameterised using an expression proposed by Borgia et al. [8].

* Corresponding author. Address: Department of Radiotherapy, Ghent University Hospital, De Pintelaan 185, 9000 Gent, Belgium.
E-mail addresses: steven.baete@ugent.be (S.H. Baete), yves.dedeene@ugent.be (Y. De Deene).
[1] Both authors contributed equally.

1090-7807/$ - see front matter © 2008 Elsevier Inc. All rights reserved.
doi:10.1016/j.jmr.2008.05.010

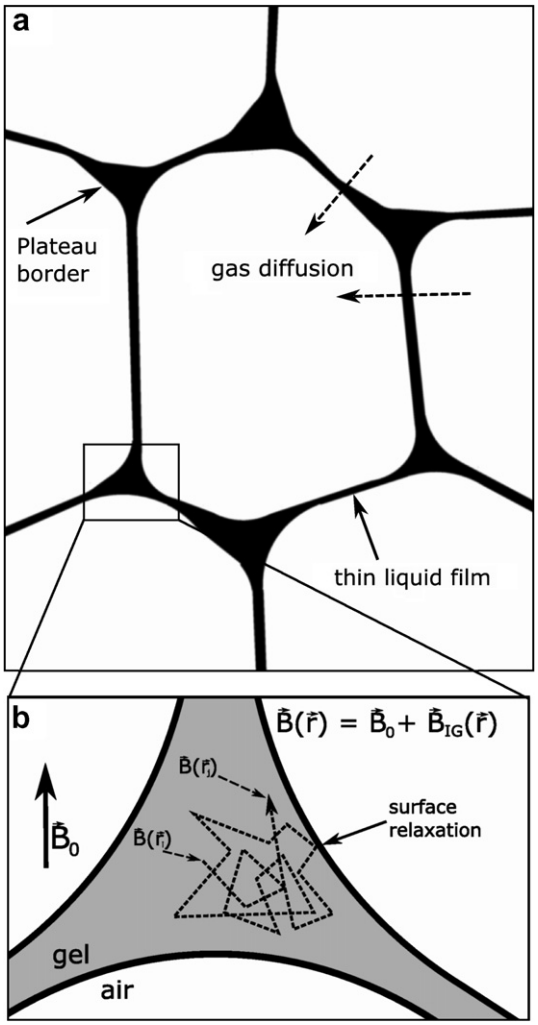

Fig. 1. (a) The porous structure of a hydrogel foam consists of thin liquid films and Plateau borders surrounding the air bubbles. Pressure differences caused by surface tension drive gas from smaller to larger bubbles. (b) Diffusing water molecule in a Plateau border. The transverse relaxation rate R_2 is increased by interactions at the gel-air interface (the surface relaxation R_{2S}) and by diffusion in the inhomogeneous magnetic field $\vec{B}_{IG}(r)$ caused by susceptibility differences (R_{2IG}).

From the fitted parameters, general correlations describing the influence of the geometric and foam composition-related properties are formulated. A semi-empirical functional relationship has been obtained for the air bubble radius and spread (standard deviation on the air bubble size) and the R_2-dispersion. Using this relation, the air bubble radius and spread can be estimated from the measured NMR R_2-dispersion of our hydrogel foams.

Foam-like pore structures have been studied using X-ray tomography (e.g. [29,30]), optical methods (e.g. [3,31–35]) and NMR microscopy (e.g. [30,36–41]). In some NMR studies contrast agents have been added to the foam composition in order to minimise the susceptibility difference between the gaseous and the liquid fraction of the foam (e.g. [36,37]).

An aqueous foam is a non-equilibrium system: the geometries and ratios of the gaseous and liquid fractions vary with time (e.g. [3,29]). Three main ageing processes govern the evolution of foam: gas diffusion across the liquid films, liquid drainage and film rupture. Gas diffusion across the liquid film alters the distribution of air bubble sizes (coarsening). Pressure differences, caused by surface tension, between air bubbles drive gas through the thin films which separate the bubbles (Fig. 1a). Some bubbles will shrink and disappear, others will initially grow, consuming the gas of neighbouring bubbles. Coarsening has been characterised by various imaging techniques ([3,29,31,33,35,37,42]). Other studies have used NMR signal intensity measurements as a function of height in foam columns to study the drainage of the liquid fraction in the foam ([42–45]).

The gelatin hydrogel foam used in this study sets in a time span of roughly one day. During gelation the gel foam will exhibit (slow) coarsening but no or little liquid drainage and film rupture due to the high amounts of gelatin in the hydrogel foam. When the gel has set (after 24–48 h), coarsening stops and the structure remains static for a long period until the gel degrades (at least 60 days when well stored [46]). The coarsening in the first few post-manufacturing hours is used here to illustrate the correlation between foam microstructure and R_2-dispersion.

In addition to the NMR measurements, the changes in microstructure related to coarsening have been observed by micro-CT (μCT) imaging [29,30]. The bubble size obtained from three dimensional micro-CT-images (μCT) is compared with the bubble size derived from R_2-measurements.

2. Materials and methods

The transverse R_2-relaxation of spins diffusing in a restricted environment is enhanced by several relaxation contributions [4,8–17,19,21,26–28]. In foam, when no external gradients are applied and the B_0-field is uniform, three contributions are important: R_{2b} (b for bulk), the intrinsic relaxation rate in the gel matrix, the surface relaxation R_{2S}, caused by collisions of diffusing spins with the boundaries of the air bubbles, and R_{2IG}, the relaxation caused by internal gradients that originate from differences in magnetic susceptibility (χ) between the gel and the gas phase. The measured R_2 will thus depend on the echo time spacing in a CPMG sequence. The R_2 as a function of the echo time spacing is called R_2-dispersion. The R_2-dispersion curve resulting from these three contributions can be fitted towards a function as discussed in Section 2.1. The latter two contributions can be simulated using an extended version of a random walk simulation as shown in Section 2.2. The foam production is discussed in Section 2.3. Sections 2.4 and 2.5 describe the MR- and μCT measurements, respectively.

2.1. R_2-dispersion fit

The variation $\Delta\omega$ of the local angular resonance frequency from the resonance frequency ω_0 in a homogeneous gel depends on the magnetic field variations caused by differences in magnetic susceptibility χ [5,8] between the gel and the gas phase of the foam. If $|\chi| \ll 1$ the field deviations are smaller than $\pm\frac{1}{2}\chi B_0$, which means that the variation in the angular frequency is limited to $\pm\frac{1}{2}\chi\omega_0$ [5,8]. The actual distribution of $\Delta\omega$ within these limits depends on the nature of the porous medium. If the porous medium is composed of relatively large pores connected by narrow channels, the Plateau borders, a substantial part of the spins is situated near the centre of a pore. In the centre of the pore the magnetic field is nearly uniform and it can be assumed that $\Delta\omega$ is very small for these spins. The other spins, situated near the edge of the pores or in the Plateau borders, will experience a highly non-uniform magnetic field (the internal gradients). The latter dipoles will experience large variations $\Delta\omega$ from the mean angular frequency ω_0. It is clear that, following this intuitive depiction, the distribution of $\Delta\omega$ will not be Gaussian. In literature [8,10,21,22] a truncated Cauchy–Lorentz distribution g of the local field B_{IG}, and correlated $\Delta\omega$, is suggested

$$g(B_{IG}) = g(B - B_0) = \frac{1}{\pi}\frac{\Delta B_{IG}}{(B_{IG} - \overline{B}_{IG})^2 + (\Delta B_{IG})^2} \quad (1)$$

with ΔB_{IG} the half width at half maximum and $\overline{B}_{IG}$ the statistical mean. The narrow mean peak in the distribution incorporates the nearly uniform local field at the centre of the pores, while the long tails show the influence of the highly inhomogeneous local field at the edges of the pores and in the Plateau borders.

If the distribution of $\Delta\omega$ is moderately narrow, the R_2-relaxation dispersion resulting from the internal gradients can be fitted by the product of two arctangent functions [8]. Including the effect of the surface relaxation R_{2S} and the intrinsic relaxation R_{2b}, by adding a constant parameter a, the expression for R_2 as a function of half of the echo time spacing $\Delta TE/2 = \tau$ is

$$R_2 = a + b\left[\frac{2}{\pi}\tan^{-1}\left(\frac{\pi}{2}\frac{\tau}{T_3}\right)\right]\left[\frac{2}{\pi}\tan^{-1}\left(\frac{2}{\pi}\frac{\tau}{T_4}\right)\right] \quad (2)$$

with b characterising the asymptotic value of the dispersion curve. The curve described by (2) has an approximately linear portion for $T_4 \ll \tau \ll T_3$. For the echo times presented in this article $\tau \ll T_3$. This means that b and T_3 cannot be determined separately. Only $B = b/T_3$ can be reliably fitted. With $\tau \ll T_3$ Eq. (2) becomes

$$R_2 = a + B\tau\left[\frac{2}{\pi}\tan^{-1}\left(\frac{2}{\pi}\frac{\tau}{T_4}\right)\right] \quad (3)$$

with B a measure for the slope of the approximately linear portion of the dispersion curve. In [5] the same functional form is found under the condition of $|\chi| \ll 1$ which is the case here. The weak field approximation, described in [14], predicts a similar function when $R_2 < \frac{D}{L^2}$ with L the length scale of the magnetic field inhomogeneities. If the maximum length scale L is taken to be the largest characteristical pore dimension (3.6 μm) R_2 should be smaller than $\approx 80\ s^{-1}$ (with $D = 1.062 \times 10^{-9}\ m^2/s$) to satisfy the weak field approximation. The R_2 values in this study fulfil this condition.

2.2. Computer simulations

The two relaxation components R_{2S} and R_{2IG} can be simulated using a random walk simulation [6,24–28]. The diffusion of random walkers representing spins in a pore structure is simulated from time $t = 0$ to time $t = TE = 2\tau$.

Collisions of diffusing spins with the interface between gel and gas phase will enhance R_2 relaxation (Fig. 1b). Each collision can be seen as a loss of magnetisation of the ensemble of diffusing spins. The enhancement of R_2 relaxation depends on the fraction of the spins close to an interface. An estimate of this fraction is given by the surface-to-volume ratio $\frac{S}{V}$ of the gel component of the foam, and the surface relaxivity ρ, a measure for magnetisation loss at the surface. The surface relaxation R_{2S}, caused by the loss in magnetisation, can be expressed as [11]

$$R_{2S} = \rho\frac{S}{V}. \quad (4)$$

The surface relaxation can be implemented in the numerical model of the random walk by counting the collisions of the random walkers with the boundaries and by attributing a specified loss of fictional proton magnetisation to each collision with the surface. Summing up the magnetisation losses for all the random walkers in the simulation `NP` during a time t as `sumrelax(`t`)`, the surface relaxation can be calculated as

$$R_{2S} = \frac{1}{t}\ln\left(\frac{\texttt{NP}}{\texttt{sumrelax}(t)}\right). \quad (5)$$

This formula can be derived by expressing the decrease in signal amplitude, due to magnetisation losses, as a relaxation rate R_{2S}.

In [25,26,28] surface relaxation is incorporated in computer simulations by using a destruction probability. At each collision of a random walker with the surface the proton magnetisation decays (i.e. the walker is destroyed) with a certain probability. This method has the disadvantage that random walkers are "lost" during the simulation. If the surface relaxivity is high this will compromise the precision of the entire diffusion simulation.

The diffusion of spins in magnetic field inhomogeneities causes phase shifts, producing extra relaxation R_{2IG}. The magnetic field inhomogeneities arise from differences in magnetic susceptibility χ of the air in the air bubbles ($\chi_{V,air} = 0.36 \times 10^{-6}$, [47]) and the gel in-between the air bubbles ($\chi_{V,H_2O} = -9.0323 \times 10^{-6}$ (20 °C), [47]). The required internal field distribution $\vec{B}_{IG}$ can be calculated with an iterative method [48,49] using a three dimensional magnetic susceptibility distribution. Calculated and theoretical magnetic field distributions for the case of a single sphere are in good agreement, within 3% deviation. Another, Fourier transform-based, method [50,51] for the calculation of field inhomogeneities gives comparable results.

The phase shift ϕ_k at time 2τ of a diffusing spin k due to an inhomogeneous magnetic field $\vec{B}_{IG}$ in a spin echo sequence is given by [4,16,27]

$$\phi_k(2\tau) = \gamma\Delta t\left[\sum_{t_l=0}^{t_l\leqslant\tau}\vec{B}_{IG}(\vec{r}_k(t_l)) - \sum_{t_l\geqslant\tau}^{t_l=2\tau}\vec{B}_{IG}(\vec{r}_k(t_l))\right] \quad (6)$$

where γ is the nuclear gyromagnetic ratio, t_l are the discrete time steps in the random walk and $\vec{r}_k(t)$ the three dimensional path of the random walker. The transverse relaxation enhancement, due to magnetic field inhomogeneities, R_{2IG} is now easily obtained by averaging the squares of the phase shifts of the ensemble of random walkers [4,5,8,17,19]

$$R_{2IG}(2\tau) = \frac{\langle(\phi_k(2\tau))^2\rangle}{2\ (2\tau)}. \quad (7)$$

This expression is valid in the Gaussian phase approximation when the phase shifts after an echo time 2τ for the various spins are either small or have a gaussian distribution. The validity of Eq. (7) will be discussed in Section 4.

In the random walk simulation special care has been taken to ensure a correct modelling of the air bubble surfaces and the interactions of random walkers with these surfaces. The air bubbles are represented as triangulated surfaces (e.g. Fig. 10a). These simplicial complexes are defined by the vertices and the edges of the triangles which shape the bubbles. When a random walker approaches a surface, it's exact collision point with the triangles is calculated and the random walker is elastically reflected in a random direction.

Two types of foam structures are used in the random walk simulations: foam structures reconstructed from μCT measurements and synthetic foam structures. Several methods exist for the reconstruction of foam structures from three dimensional image sets (e.g. [29,30,32,37,38]). The μCT-image sets are thresholded with the image processing program ImageJ (National Institutes of Health). When the films between air bubbles are not visible, they are extended in space starting from their Plateau borders. The image sets are transformed into a set of triangulated surfaces (simplicial complexes) using the program `isosurface` in Matlab (The Mathworks, Inc.). `Isosurface` transforms the ensembles of voxels forming one air bubble to a simplicial complex. A view of one of these triangulated bubble sets is shown in Fig. 10a. Notice that the bubbles are cut off at the edges of the considered volume. This may induce small discrepancies between the measured R_2 and the simulated R_2 but was found necessary to keep the computational time within reasonable limits. The synthetic foam structures are generated by randomly distributing spherical bubbles with Gaussian distributed radii. In these generated foams, the mean air bubble radius R and the standard deviation σ_R on the mean bubble radius are varied. The porosity of the synthetic foams is the same as in the foams reconstructed from the μCT-images. The air bubbles of the

synthetic foam structures are then grown to air cavities with minimal surface energy using a gradient descent algorithm (Surface Evolver [52], e.g. [32] for usage in foam reconstruction). The surfaces are transferred back to Matlab for use in the random walk simulation.

A typical random walk simulation contains 2×10^4 random walkers each performing 2×10^3 steps (stepsize 0.15 μm). Simulation results converge for stepsizes smaller than 1 μm for diffusion simulations and for stepsizes smaller than 0.3 μm for R_2 simulations.

2.3. Foam fabrication

The gel foam used here is based on a recipe described in a previous study of a lung-equivalent radiation sensitive gelatin foam [53]. The gel foams are composed of gelatin (300 Bloom, type A) [8% (w/w)], methacrylic acid (MAc) [10% (w/w)], sodiumdodecylsulphate (SDS) [0.15% (w/w)], bis[tetrakis(hydroxymethyl)phosphonium]sulphate (THPS) [10 mM], and de-ionised water [approximately 86% (w/w)]. All chemicals were purchased from Sigma–Aldrich. In the gel foam the gelatin serves as gelling agent. The methacrylic acid is used as a radiation sensitive chemical but also causes a loss of gel strength which enhances foam coarsening. Although the gelatin solution has a high foaming capacity by itself, the addition of the surfactant SDS increases the stability and homogeneity of the foam. THPS, added in a concentration of 10 mM, is used as an antioxidant and makes the gel set more rapidly preventing a rapid collapse of the foam. For the purpose of this work the gelatin fraction of the gel in [53] was decreased to induce coarsening of the foam.

The gelatin foam is fabricated by dissolving the gelatin powder in 75% of the de-ionised water at room temperature (approximately 22 °C). After swelling of the gelatin powder for about 15 min, the gelatin solution is heated to 50 °C in order to obtain a sol and left to cool down to approximately 40 °C while being magnetically stirred. MAc and SDS are dissolved in the remaining part of de-ionised water while stirring intensely and added to the gelatin solution. The gel is reheated to 36 °C. The magnetic stirrer is then removed and the gel is beaten by use of a household mixer. After approximately 3 min, a white viscous creamy foam with very small bubbles is obtained. The THPS is added while still beating the gel. After another minute, the gel foam is poured into containers (1 plastic cylindrical container of approximately 20 ml for MR imaging, 1 Minispec™ test tube containing 1 ml of foam for MR relaxometry and 1 plastic tube with a diameter of 8 mm for μCT imaging, thus all gel foam samples originate from the same batch). The containers are sealed airtight and immediately transferred to the MR and μCT-scanner. It was tested previously that none of the container materials contributed to the NMR signal.

To account for ageing of the gelatin gel [46], a fraction of the non-beaten liquid gel of the same batch was poured, before beating the gel, in an identical cylindrical container for subsequent MR imaging.

2.4. R_2-dispersion measurements

NMR imaging is performed on a 3 T scanner (Siemens Trio) equipped with a circularly polarised Helmholtz head coil using a multiple spin echo sequence with 32 equidistant echo's. A Carr–Purcell–Meiboom–Gill (CPMG) phase alternating radio-frequency pulse scheme is used. The plastic containers are scanned in the longitudinal direction (parallel to the container axis) with the following imaging parameters: repetition time (TR) 3 s, field-of-view (FOV) 180 mm, slice thickness 5 mm, matrix size (MS) 128×128 and receiver bandwidth (BW) of 352 Hz per pixel. The samples are placed in the head coil using a custom made PMMA holder that enables reproducible positioning of the samples in-between successive measurements. For the dispersion study, R_2 measurements with echo time spacings ΔTE of 8, 10, 12, 14, 16, 18 and 20 ms are performed. Each individual measurement takes 6 min 30 s resulting in a total measurement time of 45 min for one dispersion experiment. The non-beaten gelatin gel is measured with the same multiple spin echo sequence using the same imaging parameters as for the foam samples but with an echo time spacing ΔTE of 40 ms. Each hour, starting approximately 1 h after foam production, both a foam R_2-dispersion measurement and a gelatin gel R_2 measurement are performed. This measurement sequence is repeated 10 times.

All R_2-relaxation curves are fitted in Matlab, to a mono-exponential function using a maximum-likelihood χ^2-minimisation fitting algorithm [54].

The multiple spin echo sequence on the Siemens Trio is also used for ^{1}H-proton density imaging. In this case, the intercept of the R_2-relaxation curve is used as a measure for the proton density. For the foam samples, the echo time spacing ΔTE is set to 12 ms; for the gel samples ΔTE is set to 40 ms. A sample containing de-ionised water (H_20) is also added for calibration. The ^{1}H-proton density relative to water (ρ_H^w) is defined as the ratio of the hydrogen proton concentration in the sample $[H]_{sample}$ and the hydrogen proton concentration in water $[H]_{water}$ for the same atmospheric conditions [53] and is proportional to the MR signal for the echo time TE approaching 0

$$\rho_H^w = \frac{[H]_{sample}}{[H]_{water}} = \frac{\lim_{TE\to 0} S_{sample}(TE)}{\lim_{TE\to 0} S_{water}(TE)}. \quad (8)$$

R_2 dispersion curves of a gel foam sample are also measured with a 0.5 T benchtop relaxometer (Brüker Minispec™ mq20) using a multiple spin echo CPMG sequence. The measurement temperature in the relaxometer is controlled by a thermo-regulated circulating water bath. Field inhomogeneities and temperature drift are compensated by adequate positioning of the samples and by waiting for thermal equilibrium. The following measurement parameters are used: repetition time 5 s, 4 acquisitions, half echo time spacings τ from 1 ms to 13 ms with increments of 0.5 ms resulting in 23 R_2 measurements for each dispersion curve. The measurements are repeated 14 times, starting 30 min after foam production.

The intrinsic diffusion coefficient of the gelatin gel, required for the computer simulations, is measured on the relaxometer using a pulsed field gradient stimulated echo sequence (repetition time TR = 5 s) with $\Delta = 20$ ms and $\delta = 0.4$ ms. Diffusion weighted gradients with strengths linearly ranging up to 4 T/m are applied. A de-ionised water sample is used for calibration of the diffusion gradients. The diffusion coefficient is calculated according to the Stejskal–Tanner formulation [55].

2.5. μCT measurements

The X-ray μCT-scanner of the "Centre for X-ray tomography" of the Ghent University (UGCT) is used to scan a foam sample contained in cylindrical plastic tubing. The X-ray source, a FXE-160.50 dual head open type tube from Feinfocus, is equipped with a nano-transmission head and used together with a Photonic Science VHR imaging detector. The X-ray tube voltage was set at 60 kV. For each image, 295 projections with an exposure time of 0.2 ms for each projection are taken. The voxel size is 19.4 μm. A gel foam sample is imaged at different post-manufacturing time intervals, that is: 1 h 40 min, 2 h 40 min, 3 h 20 min, 6 h 20 min, 10 h 40 min and 22 h 30 min after gel foam production.

3. Results

3.1. Random walk computer simulation

Random walk simulations are performed on several synthetic foam structures in which structural and composition-related parameters are varied. While changing one property, all other properties of the foam system are kept constant. The synthetic foam structures can be more homogeneous than the fabricated foam. All simulated R_2-dispersion curves have been fitted to expression (3). In the computer simulation the different components of the R_2-relaxation, R_{2b}, R_{2S} and R_{2IG}, have been investigated independently. The effects of surface relaxivity ρ, diffusion coefficient D, magnetic susceptibility χ and the air bubble radius r and standard deviation σ_r/r on the fitted parameters a, B and T_4 are plotted in Figs. 2–4, respectively. In Fig. 2a a is fitted to a linear function of the surface relaxivity ρ

$$a = 2.5\ 10^5\ \rho + 0.6, \tag{9}$$

with ρ in [m s^{-1}]. The diffusion coefficient D affects both B and T_4. B is proportional to D, whilst T_4 is varying inversely

$$B = 1.2\ 10^{11}\ D + 440, \tag{10}$$

$$T_4 = 1.8\ 10^{-12}\ \frac{1}{D} + 3.4\ 10^{-3} \tag{11}$$

with D in [m^2 s^{-1}]. The parameter B has a quadratic dependence on the magnetic volume susceptibility χ

$$B = 7.4\ (10^6\ \chi)^2 - 49. \tag{12}$$

Figs. 2d, 3d and 4d show the fitted parameters a, B and T_4 as a function of the mean air bubble radius r and the normalised standard deviation σ_r/r of the air bubble radii. The R_{2S}-components (not shown) were found to be independent of r and σ_r/r. The parameters a, B and T_4 can be expressed as functions of r and σ_r/r (fits not shown in Figs. 2d, 3d and 4d)

$$a = 3.0 \times 10^{-4}\ \frac{1}{r} - 1.2 \times 10^{-4}\ \frac{\sigma_r}{r^2} + 0.64, \tag{13}$$

$$B = 170\ \frac{1}{\sqrt{r}} - 120\ \frac{\sqrt{\sigma_r}}{r} - 3.0 \times 10^3, \tag{14}$$

$$T_4 = -6.8 \times 10^3\ r^2 + 8.88\ r + 4.4 \times 10^{-3} \tag{15}$$

with r in [m] and σ_r/r dimensionless.

Fig. 5 shows the distributions of the local field $\vec{B}_{IG}$ as calculated by the computer simulation for synthetically generated foams with different standard deviations of the air bubble radii.

3.2. Gel and foam parameters

The diffusion coefficient D of a non-beaten gel is measured as a function of post-production time. In the first two hours post-production a slight decrease of D is observed. This decrease, although smaller than the measurement error, could be due to the gelation process of the gelatin in the gel. As only small variations in D are observed over time, the diffusion coefficient can be assumed constant. An average value for D of $1.062 \times 10^{-9} \pm 5 \times 10^{-11}$ m^2 s^{-1} is used in the computer simulations of gel foams.

Fig. 6 shows the increase of R_2 of the non-beaten gelatin gel due to ageing of the gelatin gel during the first 12 h after production. A power function,

$$R_2(t) = 0.95 t^{0.29} - 2.4 \times 10^{-3}, \tag{16}$$

is fitted to the R_2-curve. The fitted function is used to correct the R_2 dispersion curves measured at different post-manufacture times (Fig. 7) for the gelatin ageing process. The R_2 of the gelatin

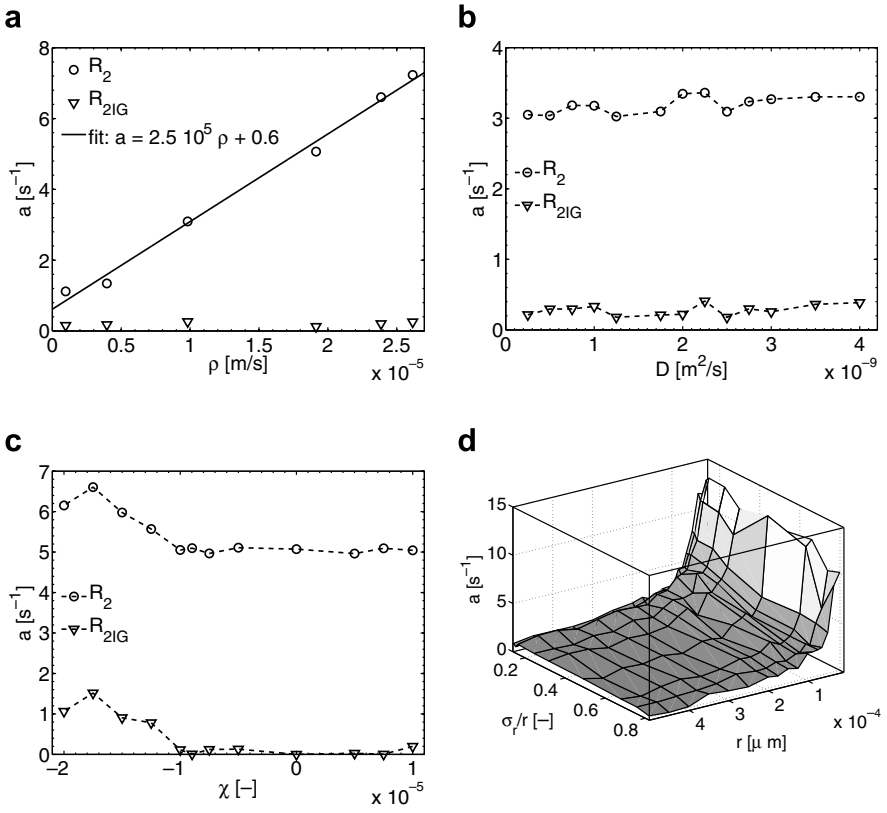

Fig. 2. Parameter a, as a function of surface relaxivity ρ (a), diffusion coefficient D (b), magnetic susceptibility χ (c) and the air bubble radius r and standard deviation σ_r/r (d), resulting from fits to Eq. (3) of simulated R_2-dispersion curves (synthetic foam structures).

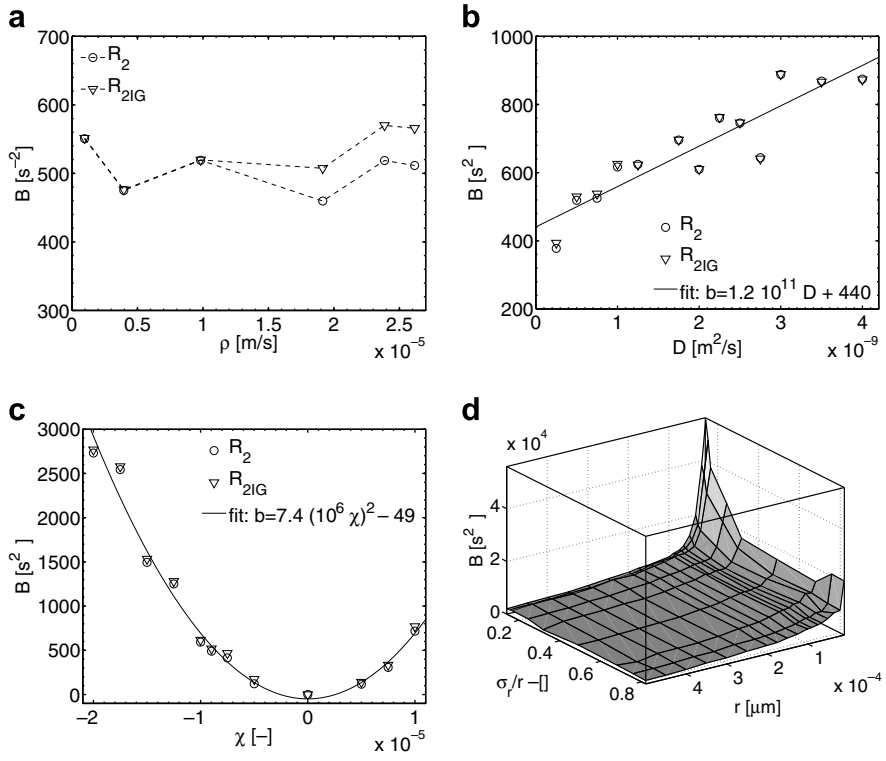

Fig. 3. Parameter B, as a function of surface relaxivity ρ (a), diffusion coefficient D (b), magnetic susceptibility χ (c) and the air bubble radius r and standard deviation σ_r/r (d), resulting from fits to Eq. (3) of simulated R_2-dispersion curves (synthetic foam structures).

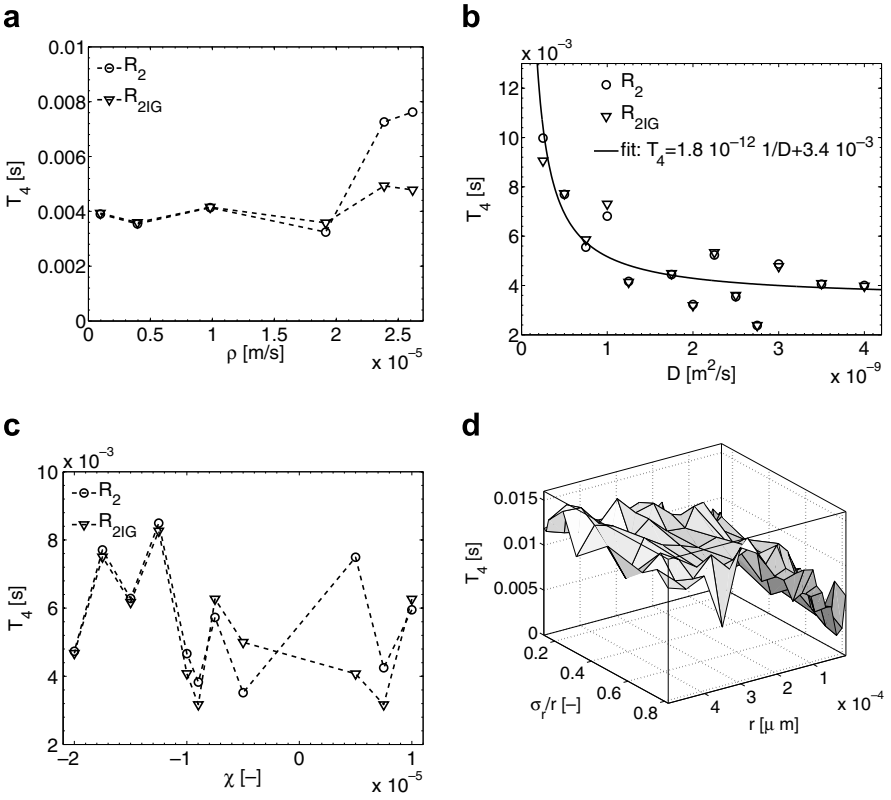

Fig. 4. Parameter T_4, as a function of surface relaxivity ρ (a), diffusion coefficient D (b), magnetic susceptibility χ (c) and the air bubble radius r and standard deviation σ_r/r (d), resulting from fits to Eq. (3) of simulated R_2-dispersion curves (synthetic foam structures).

gels at post-manufacture time $t = 0$ is used as the intrinsic relaxation rate R_{2b} of the gel foam in the computer simulations. The mean NMR ^{1}H-proton density ρ_H^w of a gel foam sample is measured using a multiple spin echo sequence. ρ_H^w is determined as 0.167. The measured foam density is consistent with earlier results [53].

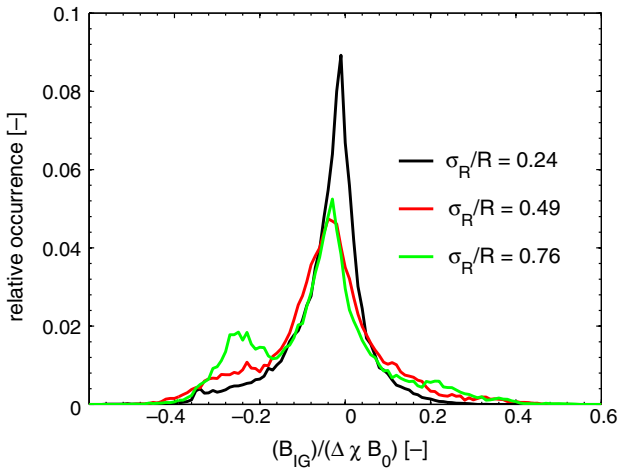

Fig. 5. Distributions of the local field $\vec{B}_{IG}$ in randomly generated foams with different standard deviations of the air bubble radii.

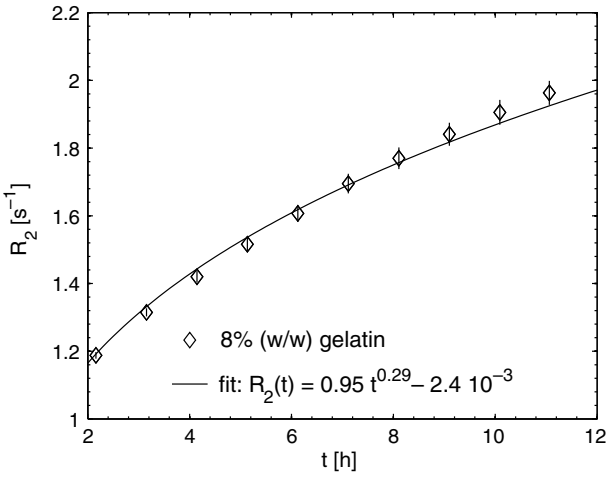

Fig. 6. R_2 of a non-beaten gelatin gel as a function of post-production time. The R_2-curve is fitted with a simple power function. (MR scanner, SE, ΔTE = 40 ms).

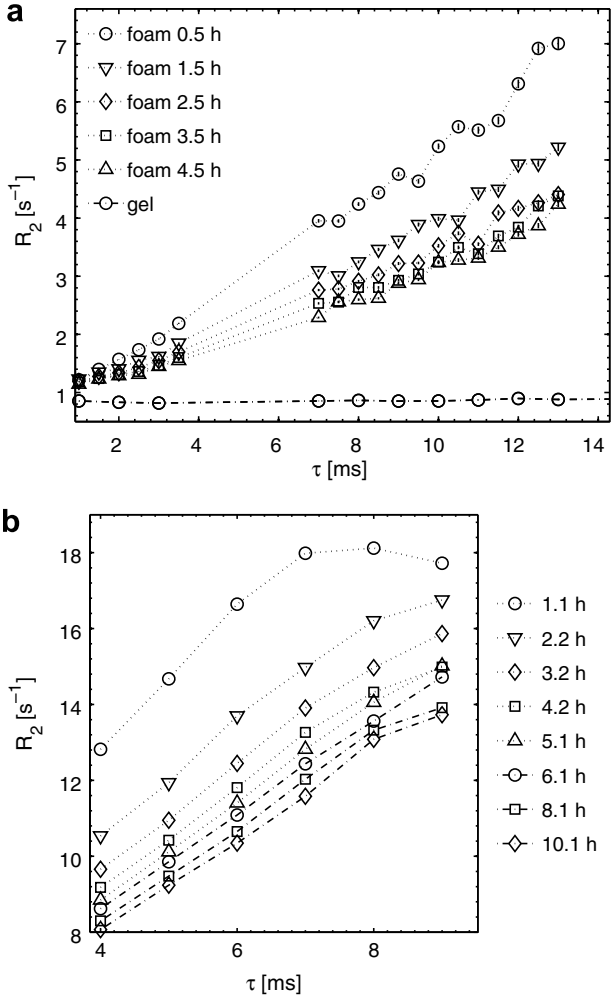

Fig. 7. R_2-dispersions of a gel foam and a gelatin gel recorded with the relaxometer (a) and the MR scanner (b) at different post-production times. The dispersion plots show the R_2 relaxation rate as a function of τ, half of the echo time spacing ΔTE. The R_2 values are compensated for the ageing of the gel (Fig. 6). For reasons of clarity only R_2-dispersion curves of foam recorded at the first few post-production hours are shown.

3.3. R_2-dispersion

R_2-dispersion curves of gel foams obtained with the relaxometer and the MR scanner as a function of time are shown in Fig. 7a and b, respectively. All dispersion curves are compensated for the ageing of the gel (Fig. 6). It is seen from Fig. 7 that the slope of the dispersion curve decreases with post-production time. The R_2-dispersion curve of the gelatin gel is added to Fig. 7a illustrating the absence of dispersion in a non-beaten gel.

Due to the low proton density ($\rho_H^w = 0.167$) only a weak signal is received from the gel foam. At larger echo time spacings the lack of signal renders image processing problematic. This may explain the saturation in R_2-dispersion at higher echo time spacings.

The R_2-dispersion curves plotted in Fig. 7b are fit to expression (3). The resulting parameters a and B are shown in Fig. 8 as a function of post-production time of the gel foam.

3.4. μCT imaging of foam

μCT-images of the same cross-section of the gel foam sample at different imaging times are shown in Fig. 9a-d. The cylindrical plastic tubing used as a container can also be seen (as a grey circle) in the images. This sequence of images (Fig. 9a–d) illustrates the coarsening process of the foam. As a result of this coarsening process, the mean air bubble radius increases while the number of air bubbles decreases with time. A 3D reconstructed μCT-image of a gel foam is shown in Fig. 9e.

A three dimensional view of one set of processed μCT-images of gel foam is shown in Fig. 10a. Fig. 10b shows the evolution of the mean radius and the standard deviation on the radius of the air bubbles in a hydrogel foam as calculated from the triangulated μCT-images. The increase of the mean radius is relatively fast in the first 5 h after fabrication and then slows down as the gelation process continues. Also in Fig. 10b, the expected [3,31,33,35,37] bubble growth of a coarsening foam according to a power law $(\bar{r} - \bar{r}_0) = k(t - t_0)^z$ is fitted to the μCT measured mean air bubble radii $\bar{r}$

$$\bar{r} = 20(t - 1.6)^{0.4} + 160, \tag{17}$$

with $\bar{r}$ in [μm] and t in [h].

Fig. 11 shows a comparison of random walk simulated R_2-dispersion curves with the measured R_2-dispersions (of Fig. 7b). The foam structures derived from the μCT images are used as input in these computer simulations.

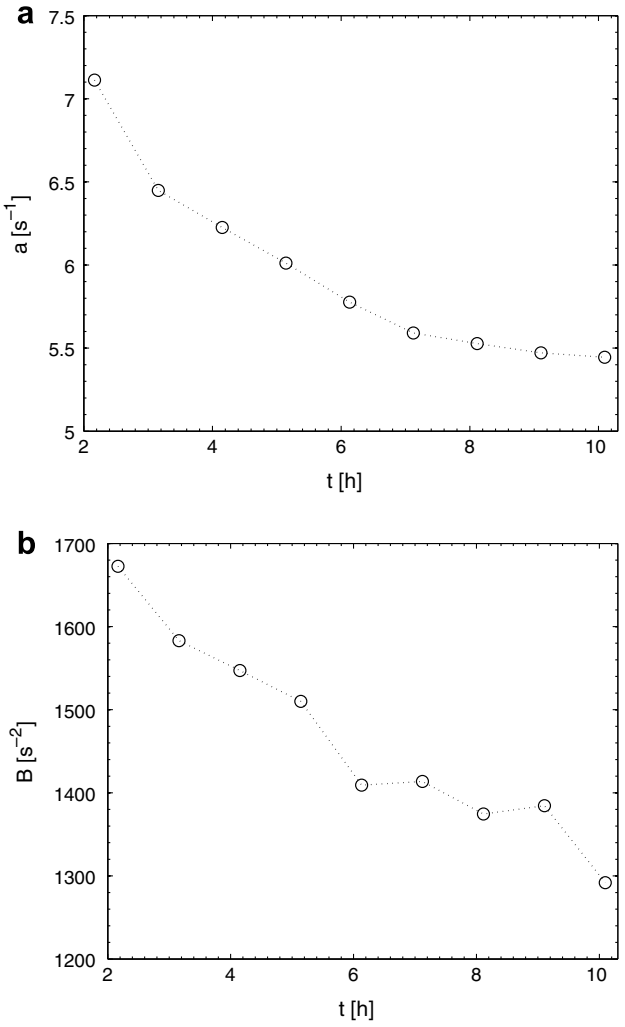

Fig. 8. Parameters (a) a and (b) B resulting from a fit to Eq. (3) of the R_2-dispersion curves shown in Fig. 7b as a function of post-production time of the gel foam.

The above mentioned correlations (9)–(15), derived from analysing simulations on synthetic foams, enable the prediction of the mean and standard deviation of the air bubble radii from measured R_2-dispersion curves. The bubble radius r (and standard deviation σ_r) of a foam can be determined from the measured R_2-dispersion parameters a and B by use of the inverse of the Eqs. (9)–(15). The system parameters such as surface relaxivity ρ, diffusion coefficient D and magnetic susceptibility χ have to be determined independently. To illustrate the applicability of this method, the air bubble radii (and standard deviation) derived from R_2-dispersion measurements on a coarsening gel foam are compared with the radii directly derived from the μCT-images (Fig. 12).

4. Discussion

In this study, it is shown that R_2-dispersion computer simulations in synthetic foams can be used to correlate the R_2-dispersion curve with the bubble radius r (and the standard deviation σ_r). The empirically found correlations of the R_2-dispersion coefficients a, B and T_4 are listed in Eqs. (13)–(15). The correlations of the R_2-dispersions coefficients as shown in Figs. 2–4 are listed in Eqs. (9)–(12). From the simulations it can be concluded that the surface relaxivity ρ only affects the constant part a of the dispersion curve, whereas the difference in magnetic susceptibility χ only affects the slope of the linear portion of the dispersion curve B. Both the slope B and the beginning time T_4 of the linear portion of the dispersion curve are affected by the diffusion coefficient D. As the diffusion coefficient increases, the mean diffusion distance within a certain diffusion time of random walkers increases. The random walkers will sense a large variety of magnetic fields, leading to an earlier and increased dephasing. Similarly, increasing the susceptibility difference will increase the magnitude of the magnetic field inhomogeneities, also leading to increased dephasing. The quadratic dependence of B on χ is in accordance to earlier findings [8,14]. Changes in the mean and standard deviation of the air bubble radii affect both the constant part, the slope and the beginning time of the linear portion of the dispersion curve. The constant part of the R_2-dispersion curve a is affected due to changes in surface-to-volume ratios which influence the surface relaxation R_{2S} (4).

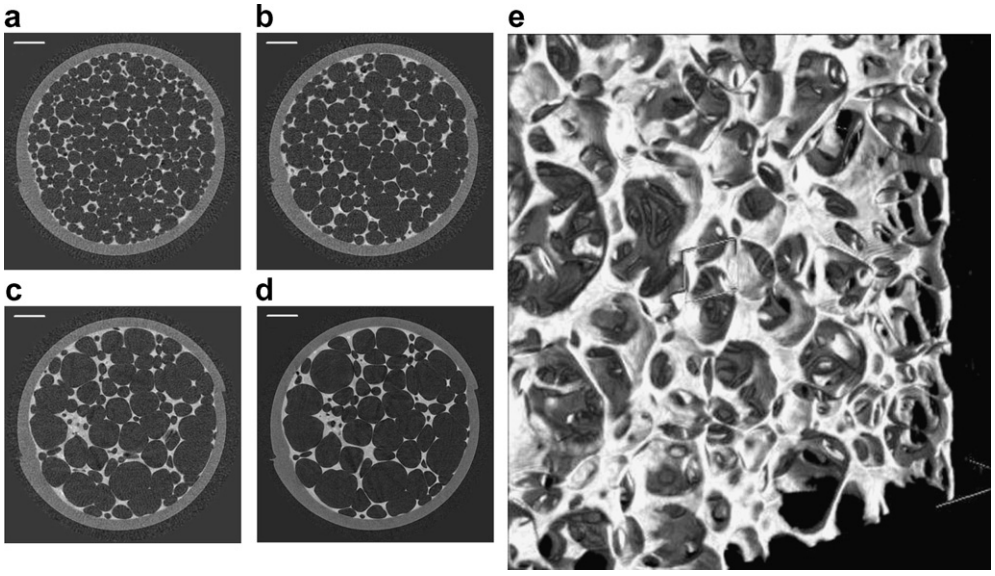

Fig. 9. (a–d) μCT-images of a cross-section of plastic tubing filled with gel foam. The images are taken at different post-production times, that is: (a) 1 h 40 min, (b) 3 h 25 min, (c) 12 h 35 min and (d) 22 h 30 min after gel foam production. The white bar on each cross-section has a length of 1.165 mm. (e) 3D μCT-image of a gel foam.

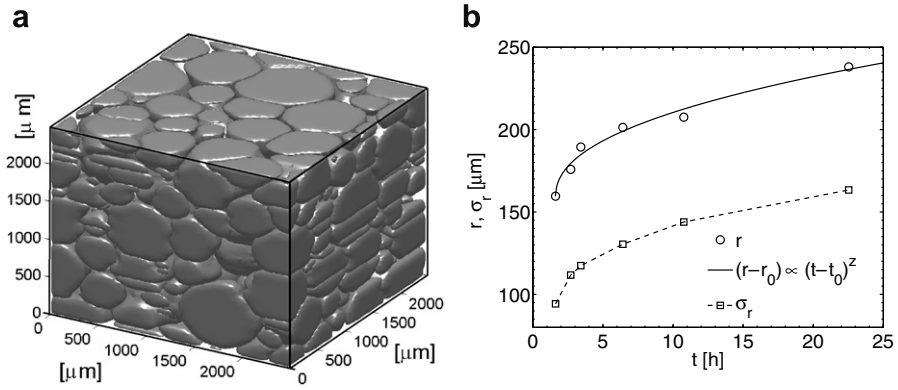

Fig. 10. (a) Three dimensional view of one set of processed μCT-images of gel foam [1 h 40 post-production]. Each air bubble is represented by a triangulated surface. (b) Mean radius (r) and standard deviation on the radius (σ_r) of the air bubbles of a gel foam as a function of post-production time derived from the μCT-images. The triangulated surfaces, shown in (a), are used to calculate the air bubble radii. The expected power law growth [3,31,33,35,37] of the mean air bubble radius r of a coarsening foam is fitted.

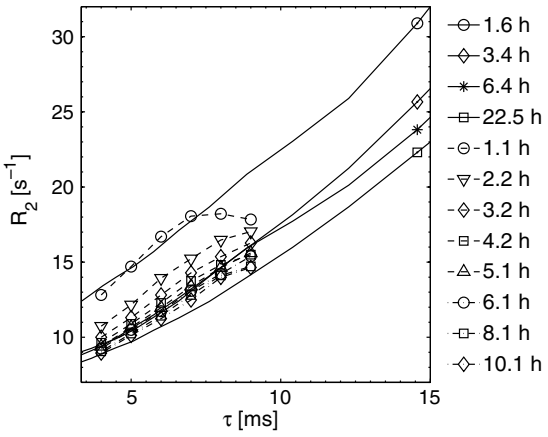

Fig. 11. Measured (dotted lines) and simulated (full lines) R_2-dispersions of a gel foam at different post-production times. Random walk simulations are performed with 10^4 random walkers (time step 3.3 μs) on a gel foam structure derived from μCT imaging.

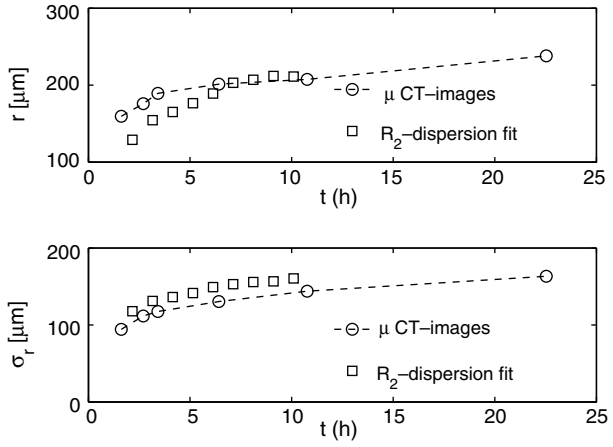

Fig. 12. Comparison of the mean (r) and standard deviation (σ_r) of the air bubble radii of a gel foam as derived from μCT measurements (Fig. 10b) and the mean and standard deviation of the air bubble radii as calculated starting from the fitted parameters a and B (Fig. 8) using the correlations (9)–(15) found by computer simulations.

When scaling a structure with a characteristic dimension x, the surface scales with a factor x^2 and the volume scales with a factor x^3. The surface-to-volume ratio then scales as $\frac{1}{x}$. This behaviour can also be found in the empirical function (13). The second term in (13) accounts for the influence of the standard deviation σ_r of the air bubble radii. If σ_r increases, the fraction of small bubbles, filling the larger pore spaces, will increase. Due to this effect the surface-to-volume ratio will increase, increasing the surface relaxation R_{2S} (4). Scaling a structure also influences the magnetic field inhomogeneities induced in the structure due to susceptibility differences. Eq. (14) gives the relation between the slope of the dispersion curve (the parameters B) and the mean and standard deviation of the air bubble radii. Eq. (15) gives the relation between the beginning of the dispersion curve (the parameter T_4) and the mean and standard deviation of the air bubble radii.

The distribution of the local field $\vec{B}_{IG}$ (Fig. 5) is a Cauchy–Lorentz distribution with a small peak and long tails as suggested in literature [8,10,21,22]. With increasing standard deviation of the air bubble radii, corresponding with a relatively larger fraction of small bubbles, a second smaller peak occurs left from the main peak in the distribution of the local field. This peak is attributed to the contribution of the small pores [22].

Expression (7) for the calculation of the enhancement of the transverse relaxation due to magnetic field inhomogeneities is valid in the Gaussian phase approximation [4,5,8,17,19]. This is when the phase shifts at echo time for the various spins are either small or have a gaussian distribution. The phase shift distributions of the random walkers in the computer simulation have been recorded. The distribution of the phase shifts is rather a Cauchy–Lorentz distribution than a Gaussian distribution, but all phase shifts are small. The validity of expression (7) has been checked by comparing the simulation results using (7) with the simulation results using a more general formulation (e.g. [27]). The difference in simulation results from both formulations is less than 1%. We conclude that, for this type of simulated porous medium, expression (7) can be used.

The MR measurements of R_2 dispersion curves (Fig. 7) show that the transverse relaxation rate R_2 increases with increasing echo time in a foam structure. R_2-dispersion is clearly observed in gelatin gel foam. The gel, used to make the gel foam, does not exhibit any R_2-dispersion as can be seen from Fig. 7a. All R_2-dispersion effects are related to the foam microstructure. The mean air bubble radius of the foam increases with time (Fig. 10b) and the slope of the R_2 dispersion curves decreases illustrating the relation between the bubble size and the R_2-dispersion. The R_2 value of a foam microstructure is thus related to the characteristical dimensions of the air bubbles. For the broader context of porous media this has been described in several theoretical models [5,8,9,11–15,17–19], and has also been experimentally observed (e.g. [6,20,21,44]).

The R_2-dispersion curves measured with the relaxometer (Fig. 7a) and the MR scanner (Fig. 7b) are in accordance. The difference in absolute R_2 values for both machines can be partly explained by the difference in magnetic field strength of both NMR systems. The field strength of the relaxometer is 0.47 T and that of the MR scanner is 3 T. However a quadratic dependence of R_{2IG} on the magnetic field strength is expected [8], whereas in Fig. 7 the scaling between the R_2 values measured with the relaxometer (Fig. 7a) and the scanner (7b) is less than the square of the corresponding magnetic field ratios. This inconsistent scaling of R_{2IG} with the magnetic field strength can be attributed to the significantly higher field inhomogeneities in the relaxometer as compared to the MR scanner. Simulated and NMR measured R_2-dispersion curves for gel foam are in good agreement (Fig. 11) illustrating the feasibility to use R_2-dispersion plots to predict microstructure properties.

Gel ageing [46] and foam coarsening are counteracting effects. R_2 increases with time due to gel ageing (Fig. 6) while R_2 decreases due to foam coarsening (Fig. 7). The decrease in R_2 due to foam coarsening is larger than the increase in R_2 due to gel ageing. The R_2-dispersion curves have been corrected for the gel ageing effect for comparison with synthetic foam R_2-dispersion curves.

The R_2-dispersion curves, measured with the MR scanner (Fig. 7b), are fitted to Eq. (3). The fitting results are summarised in Fig. 8. The beginning time of the linear portion of the dispersion curve is constant at 2.6 ± 0.1 ms. Both parameters a and B decrease with increasing time indicating increasing air bubble radii (see Eqs. (13) and (14)).

The μCT-image sets (Fig. 9) show that the air bubbles in the gel foam have evolved from a spherical shape, but have not yet reached a full polyhedral shape. The large gelatin fraction in the gel foam prevents excessive drainage and coarsening effects which would lead to polyhedrally shaped air bubbles. In the μCT-images no film ruptures are noticed and the liquid fraction of the foam remains constant at $0.166 \pm 1 \times 10^{-3}$ during the entire imaging period (1 h 40 min–22 h 30 min post-production). The 2D μCT-slices in Fig. 9 clearly show coarsening of the gel foam. The smaller air bubbles disappear while the larger air bubbles grow with time. The coarsening of the foam can be followed in three dimensions. This is possible because of the slower process of coarsening in comparison to the imaging time. The foam images in Fig. 9 are similar to images obtained in other studies [29,31,36–38,41,40].

The three dimensional image sets produced by μCT-imaging can be used to determine geometrical microstructure parameters of the gel foams studied here. The evolution of mean air bubble radii is summarised in Fig. 10b.

Coarsening has been described in numerous publications (e.g. [3,29,31,33,35,37,42]). In foam, a power law scaling behaviour $(\bar{r} - \bar{r}_0) \propto (t - t_0)^z$ of the mean air bubble radii $\bar{r}$ is expected [3,31,33,35,37]. A dry foam is expected to exhibit a growth factor $z = \frac{1}{3}$, a wet foam $z = \frac{1}{2}$ [31]. The growth exponent z for the gel foam amounts to 0.4 ± 0.2 which corresponds to an intermediate foam.

The set of Eqs. (9)–(15), derived by computer simulations using synthetic foam structures, can be used to calculate the mean and the standard deviation of the air bubble radii starting from the fitted parameters a and B of the measured R_2-dispersion curves (Fig. 8). This is done by inverting Eqs. (9)–(15). The R_2-derived air bubble radii and standard deviation (Fig. 12) are in agreement with the air bubble radii and standard deviation obtained from the μCT-images (Fig. 10b). The deviations in air bubble radii in the first post-production hours can be attributed to small air bubbles that were not identified from the μCT-images. The higher standard deviations calculated from the R_2-dispersion curves also point in this direction.

The results in Fig. 12 show the ability to determine foam structure properties from R_2-dispersion measurements in this gel foam. In general, it is expected that for a well characterised class of foam structures it is possible, by use of computer simulations, to derive a correlation between air bubble radii and R_2-dispersion. These results illustrate the potential of deriving the size of alveoli in lung tissue. The method can also be useful in food science. A potential drawback of the method is the need to determine system parameters such as the surface relaxivity ρ, the diffusion coefficient D and the magnetic susceptibility χ independently.

The intrinsic diffusion coefficient of the gel fraction of the gel foam is assumed to be equal to the diffusion coefficient of the non-beaten gel. The measured apparent diffusion coefficient will be smaller due to the geometrical confinement in the porous structure. The foam structure studied here is, at echo times larger than 7 ms, in a fast exchange limit. The mean diffusive displacement ($d = \sqrt{6Dt}$, with t the diffusion time, d ranging from 6.7 μm at $t = 7$ ms to 14 μm at $t = 31$ ms) is large compared to the pore dimensions (characteristical dimension of the pores ranges from 2.1 μm to 3.6 μm). In the literature (e.g. [12,15,18]) three relaxation regimes are distinguished: the free diffusion, localisation and motionally averaging regime depending on three length scales $L_D = \sqrt{D_0 \tau}$ (diffusion length), $L_g = \left(\frac{D_0}{\gamma \bar{g}}\right)^{\frac{1}{3}}$ (dephasing length, $\bar{g}$ is the r.m.s. average of the internal gradients) and L_S (a characteristical length for the system, in this case the mean equivalent radius of the gel pores). For this gel foam system the diffusion length scale L_D varies from 1.6 to 6.3 μm, the dephasing length is 6.3 μm (for a foam system with mean bubble radius 150 μm) and the system length varies between 2.1 and 3.6 μm (the characteristical pore dimensions). Additionally the characteristical length scale for surface relaxation $L_\rho = \frac{D_0}{\rho}$ is 130 μm ($\rho = 8.1$ μm/s). These length scales place the gel foam system in the transition region between the free diffusion regime ($L_D < L_S < L_G \ll L_\rho$, small τ) and the motionally averaging regime ($L_S < L_D < L_G \ll L_\rho$, large τ).

5. Conclusions

R_2-dispersion measurements can be used to probe the underlying microstructure of aqueous biphasic media consisting of components with surface relaxation and/or different magnetic susceptibilities. In this study the R_2-dispersion of a hydrogel foam is measured and simulated. Correlations between R_2-dispersion and mean air bubble radius are found. Simulated and measured R_2-dispersion curves are in agreement. As a proof of concept, the change in air bubble size during coarsening has been determined by NMR R_2-dispersion measurements and verified against the air bubble size derived by micro-CT imaging showing a good correspondence.

Acknowledgments

This research is supported by Grant # 01J13507 from the BOF-Ghent University. The X-ray μCT-scanner of the "Centre for X-ray tomography" is supported by the BOF-Ghent University. The authors are thankful to Bart Truyens for the construction of a sample holder for the Trio scanner.

References

[1] R. Christman, D. Ailion, T. Case, C. Durney, A. Cutillo, S. Shioya, K. Goodrich, A. Morris, Comparison of calculated and experimental nmr spectral broadening for lung tissue, Magn. Res. Med. 35 (1996) 6–13.
[2] C. Durney, A. Cutillo, D. Ailion, Magnetic resonance behavior of normal and diseased lungs: spherical shell model simulations, J. Appl. Physiol. 88 (2000) 1155–1166.
[3] D. Weire, S. Hutzler, The Physics of Foam, Clarendon Press, Oxford, 1999.

[4] C. Neuman, Spin echo of spins diffusing in a bounded medium, J. Chem. Phys. 60 (11) (1974) 4508–4511.
[5] R.J.S. Brown, P. Fantazzini, Conditions for initial quasi-linear $t(2)(-1)$ versus tau for Carr–Purcell–Meiboom–Gill nmr with diffusion and susceptibility differences in porous-media and tissues, Phys. Rev. B 47 (22) (1993) 14823–14834.
[6] R. Weisskoff, C. Zuo, J. Boxerman, B. Rosen, Microscopic susceptibility variation and transverse relaxation—theory and experiment, Magn. Res. Med. 31 (1994) 601–610.
[7] M.D. Hurlimann, K.G. Helmer, L.L. Latour, C.H. Sotak, Restricted diffusion in sedimentary-rocks—determination of surface-area-to-volume ratio and surface relaxivity, J. Magn. Reson. Ser. A 111 (2) (1994) 169–178.
[8] G. Borgia, R. Brown, P. Fantazzinni, Scaling of spin-echo amplitudes with frequency, diffusion coefficient, pore size, and susceptibility difference for the NMR of fluids in porous media and biological tissues, Phys. Rev. E 51 (1995) 2104–2114.
[9] R. Kleinberg, Utility of NMR T2 distributions, connection with capillary pressure, clay effect, and determination of the surface relaxivity parameter ρ_2, Magn. Res. Imaging 14 (1996) 761–767.
[10] G. Borgia, R. Brown, P. Fantazzini, The effect of diffusion and susceptibility differences on t−2 measurements for fluids in porous media and biological tissues, Magn. Res. Imaging 14 (1996) 731–736.
[11] W. Slijkerman, J. Hofman, Determination of surface relaxivity from NMR diffusion measurements, Magn. Res. Imaging 16 (1998) 541–544.
[12] P.N. Sen, A. Andre, S. Axelrod, Spin echoes of nuclear magnetization diffusing in a constant magnetic field gradient and in a restricted geometry, J. Chem. Phys. 111 (14) (1999) 6548–6555.
[13] J.H. Jensen, R. Chandra, Strong field behavior of the nmr signal from magnetically heterogeneous tissues, Magn. Reson. Med. 43 (2) (2000) 226–236.
[14] J.H. Jensen, R. Chandra, Nmr relaxation in tissues with weak magnetic inhomogeneities, Magn. Reson. Med. 44 (1) (2000) 144–156.
[15] S. Axelrod, P.N. Sen, Nuclear magnetic resonance spin echoes for restricted diffusion in an inhomogeneous field: methods and asymptotic regimes, J. Chem. Phys. 114 (15) (2001) 6878–6895.
[16] K. Dunn, Enhanced relaxation in porous media due to internal field gradients, J. Magn. Res. 156 (2002) 171–180.
[17] L.J. Zielinski, P.N. Sen, Combined effects of diffusion, nonuniform-gradient magnetic fields, and restriction on an arbitrary coherence pathway, J. Chem. Phys. 119 (2) (2003) 1093–1104.
[18] G.Q. Zhang, G.J. Hirasaki, Cpmg relaxation by diffusion with constant magnetic field gradient in a restricted geometry: numerical simulation and application, J. Magn. Reson. 163 (1) (2003) 81–91.
[19] L.J. Zielinski, Effect of internal gradients in the nuclear magnetic resonance measurement of the surface-to-volume ratio, J. Chem. Phys. 121 (1) (2004) 352–361.
[20] A. Radlinski, M. Ioannidis, A. Hinde, M. Hainbuchner, M. Baron, H. Rauch, S. Kline, Angrstrom-to-millimeter characterization of sedimentary rock microstructure, J. Colloid Interface Sci. 274 (2004) 607–612.
[21] P. Fantazzinni, R. Brown, Initially linear echo-spacing dependence of 1/T2 measurements in many porous media with pore-scale inhomogeneous fields, J. Magn. Res. 177 (2005) 228–235.
[22] Q. Chen, A. Marble, B. Colpitts, B. Balcom, The internal magnetic field distribution, and single exponential magnetic resonance free induction decay, in rocks, J. Magn. Res. 175 (2005) 300–308.
[23] N.V. Lisitza, W.S. Warren, Y.Q. Song, Study of diffusion in erythrocyte suspension using internal magnetic field inhomogeneity, J. Magn. Reson. 187 (2007) 146–154.
[24] B. Balinov, B. Jönsson, P. Linse, O. Söderman, The NMR self-diffusion method applied to restricted diffusion simulation of echo attenuation from molecules in spheres and between planes, J. Magn. Res. A 104 (1993) 17–25.
[25] P. Sen, L. Schwartz, P. Mitra, B. Halperin, Surface relaxation and the long-time diffusion coefficient in porous media: periodic geometries, Phys. Rev. B 49 (1) (1994) 215–225.
[26] D.J. Bergman, K.J. Dunn, L.M. Schwartz, P.P. Mitra, Self-diffusion in a periodic porous-medium—a comparison of different approaches, Phys. Rev. E 51 (4) (1995) 3393–3400.
[27] A. Duh, A. Mohoric, J. Stepisnik, Computer simulation of the spin-echo spatial distribution in the case of restricted self-diffusion, J. Magn. Res. 148 (2001) 257–266.
[28] E. Toumelin, C. Torres-Verdin, B. Sun, K.J. Dunn, Random-walk technique for simulating nmr measurements and 2d nmr maps of porous media with relaxing and permeable boundaries, J. Magn. Reson. 188 (2007) 83–96.
[29] J. Lambert, I. Cantat, R. Delannay, A. Renault, F. Graner, J.A. Glazier, I. Veretennikov, P. Cloetens, Extraction of relevant physical parameters from 3d images of foams obtained by X-ray tomography, Colloids Surf. A—Physicochem. Eng. Aspects 263 (1–3) (2005) 295–302.
[30] D.A.G. von der Schulenburg, M. Paterson-Beedle, L.E. Macaskie, L.F. Gladden, M.L. Johns, Flow through an evolving porous media-compressed foam, J. Materials Sci. 42 (16) (2007) 6541–6548.
[31] D.J. Durian, D.A. Weitz, D.J. Pine, Scaling behavior in shaving cream, Phys. Rev. A 44 (12) (1991) R7902–R7905.
[32] C. Monnereau, M. Vignes-Adler, Dynamics of 3d real foam coarsening, Phys. Rev. Lett. 80 (23) (1998) 5228–5231.
[33] S.A. Magrabi, B.Z. Dlugogorski, G.J. Jameson, Bubble size distribution and coarsening of aqueous foams, Chem. Eng. Sci. 54 (18) (1999) 4007–4022.
[34] M.R. Fetterman, E. Tan, L. Ying, R.A. Stack, D.L. Marks, S. Feller, E. Cull, J.M. Sullivan, D.C. Munson, S.T. Thoroddsen, D.J. Brady, Tomographic imaging of foam, Optics Express 7 (5) (2000) 186–197.
[35] A.M. Ganan-Calvo, J.M. Fernandez, A.M. Oliver, M. Marquez, Coarsening of monodisperse wet microfoams, Appl. Phys. Lett. 84 (24) (2004) 4989–4991.
[36] B.A. Prause, J.A. Glazier, S.J. Gravina, C.D. Montemagno, 3-dimensional magnetic-resonance-imaging of a liquid foam, J. Phys. Condensed Matter 7 (40) (1995) L511–L516.
[37] C.P. Gonatas, J.S. Leigh, A.G. Yodh, J.A. Glazier, B. Prause, Magnetic-resonance images of coarsening inside a foam, Phys. Rev. Lett. 75 (3) (1995) 573–576.
[38] C.A. Baldwin, A.J. Sederman, M.D. Mantle, P. Alexander, L.F. Gladden, Determination and characterization of the structure of a pore space from 3d volume images, J. Colloid Interface Sci. 181 (1) (1996) 79–92.
[39] B. Chauvaux, J.M. Dereppe, R. Huis, Micro-imaging by magnetic resonance on flexible polyurethane foams, Magn. Reson. Imaging 14 (7–8) (1996) 937–939.
[40] K. Kose, 3d nmr imaging of foam structures, J. Magn. Reson. Ser. A 118 (2) (1996) 195–201.
[41] M. Szayna, R. Voelkel, Nmr microscopy of polyurethane foams, Solid State Nucl. Magn. Reson. 15 (2) (1999) 99–102.
[42] B. Hills, Magnetic Resonance Imaging in Food Science, Wiley InterScience, New York, 1998.
[43] R.A. Assink, A. Caprihan, E. Fukushima, Density profiles of a draining foam by nuclear magnetic-resonance imaging, Aiche J. 34 (12) (1988) 2077–2079.
[44] M.J. McCarthy, Interpretation of the magnetic-resonance-imaging signal from a foam, Aiche J. 36 (2) (1990) 287–290.
[45] G. Pilhofer, H.-C. Lee, M. McCarthy, P. Tong, J. German, Functionality of milk fat on foam formation and stability, J. Dairy Sci. 77 (1993) 55–63.
[46] Y. De Deene, P. Hanselaer, C. De Wagter, E. Achten, W. De Neve, An investigation of the chemical stability of a monomer/polymer gel dosimeter, Phys. Med. Biol. 45 (2000) 859–878.
[47] J. Schenck, The role of magnetic susceptibility in magnetic resonance imaging: MRI magnetic compatibility of the first and second kinds, Med. Phys. 23 (6) (1996) 815–850.
[48] R. Bhagwandien, R. van Ee, R. Beersma, C. Bakker, M. Moerland, J. Lagendijk, Numerical analysis of the magnetic field for arbitrary magnetic susceptibility distributions in 2D, Magn. Res. Imaging 10 (1992) 299–313.
[49] R. Bhagwandien, M. Moerland, C. Bakker, R. Beersma, J. Lagendijk, Numerical analysis of the magnetic field for arbitrary magnetic susceptibility distributions in 3D, Magn. Res. Imaging 12 (1994) 101–107.
[50] J. Marques, R. Bowtell, Application of a Fourier-based method for rapid calculation of field inhomogeneity due to spatial variation of magnetic susceptibility, Concept. Magn. Res. B 25B (2005) 65–78.
[51] K. Koch, X. Papademetris, D. Rothman, R. de Graaf, Rapid calculations of susceptibility-induced magnetostatic field perturbations for in vivo magnetic response, Phys. Med. Biol. 51 (2006) 6381–6402.
[52] K. Brakke, The surface evolver, Exp. Math. 1 (1992) 141–165.
[53] Y. De Deene, K. Vergote, C. Claeys, C. De Wagter, Three dimensional radiation dosimetry in lung-equivalent regions by use of a radiation sensitive gel foam: proof of principle, Med. Phys. 7 (2006) 2586–2597.
[54] Y. De Deene, R. Van de Walle, E. Achten, C. De Wagter, Mathematical analysis and experimental investigation of noise in quantitative magnetic resonance imaging applied in polymer gel dosimetry, Signal Process. 70 (1998) 85–101.
[55] E. Stejskal, J. Tanner, Spin diffusion measurements: spin echoes in the presence of a time-dependent field gradient, J. Chem. Phys. 42 (1965) 288–292.